

An experimentally validated electro-thermal EV battery pack model incorporating cycle-life aging and cell-to-cell heterogeneity

Joseph N. E. Lucero

Dept. of Chemistry, Stanford University

Vivek A. Sujan

National Transportation Research Center, Oak Ridge National Laboratory

Simona Onori

Dept. of Energy Sciences & Engineering, Stanford University

Applied Energy Division, Energy Science Directorate – SLAC National Accelerator Laboratory

Abstract—Over the past decade, there has been increasing interest in using lithium-ion batteries across a wide variety of applications, particularly in electric vehicles and grid-energy storage. In order to meet the power and energy demands of these applications, a single battery cell is often insufficient: battery packs composed of hundreds to thousands of interconnected cells must be constructed. The electrical and thermal connections made between cells during assembly introduce additional complexity in terms of interconnect configuration, cell-to-cell heterogeneity effects, and thermal interactions between the cells of the pack. To investigate these effects, in this article we construct a battery pack model composed of 192 cells with a configuration based on the battery pack of a first-generation Nissan Leaf, where we simulate the electrical, thermal, and aging dynamics of every cell in the battery pack. The model is calibrated and validated with experimental data from [1]. Using this model, we show that, in the presence of “weaker” cells with reduced capacity, “stronger” cells in the pack with higher capacity accommodate their weaker partners, leading to a reduced sensitivity of the battery pack’s output voltage to the heterogeneities, at the expense of a reduced lifetime of the higher capacity cells in the pack resulting in a higher level of aging for the pack overall.

I. INTRODUCTION

Prompted by increasing concerns over pollution and greenhouse gas emissions, many automotive companies are increasingly looking to transition away from traditional internal-combustion engine vehicles powered by fossil fuels and towards electrified powertrains powered by Li-ion batteries [2]. These battery electric vehicles (BEVs) offer overall higher efficiencies and have a lower overall carbon footprint relative to internal-combustion vehicles [3]. Li-ion batteries have come to be the predominant battery technology used in the EV application due to its superior performance in both capacity and power relative to other battery types [4].

In these applications, to meet the required power and energy requirements, hundreds to thousands of battery *cells* must be connected together in a battery *pack*. Generally, cells are first connected together to form *battery module* and modules are subsequently connected together to form a pack. Sensors for voltage, current, and temperature can be placed at various levels of this hierarchy to enable monitoring of the battery state [5]. To maximize efficiency and reliability of these battery packs, cell-to-cell consistency and thermal

uniformity are known to be important [6]; however, the literature surrounding the modeling of battery packs is sparse. In particular, the creation and calibration of efficient models that are able to accurately predict the electro-thermal dynamics of battery packs throughout the entirety of the pack’s life, is hindered by lack of publicly available battery module/pack data.

There are two traditional approaches that are generally used by battery system designers to model/predict battery-cell dynamics: equivalent-circuit models (ECMs) and physics-based models (PBMs) [7]. ECMs provide a simple and computationally inexpensive model that captures the voltage dynamics of the battery but it is a purely empirical approach based on experimentally-collected data. This approach is essentially a curve-fitting process and thus cannot be reliably used for extrapolation into operating regimes for which the data used to identify the model does not cover. In contrast, PBMs allow for enhanced monitoring and prediction of the internal battery cell mechanisms, but have a more complex mathematical structure and generally require more computational time to simulate. Since PBMs model the physical processes happening within the cell, these models can be more reliably extrapolated into operating regions that may not be covered by experimental data at the cost of increased model complexity and computational cost.

Both ECMs and PBMs can also be augmented with models that capture the thermal and aging dynamics the battery cell. To model the temperature changes of the battery cell during its operation, ECM and PBM models are often augmented with a lumped-parameter thermal models. To capture the capacity and power fade of the battery cell, ECM models are often augmented by semi-empirical models calibrated using experimental data [8], [9] Similarly, PBM models are often augmented with expressions for the growth dynamics of the solid-electrolyte interface layer, and lithium-plating dynamics [10].

Both modeling approaches can successfully capture, to a high degree of accuracy, the electric and thermal response of battery cells under different loads; however, these methods do not scale to the pack level without an accompanying increase in computational cost. In control-oriented applications, such

as battery management systems (BMS) in EVs, such an increase is generally undesirable as it increases latency, lowering the quality of state estimation. As such, a commonly invoked assumption is that of pack *modularity*: the dynamics of the pack can be determined from the dynamics of an individual cell [11]. By using this assumption, any cell-to-cell heterogeneities present within the pack are neglected and the dynamics of the pack can be reduced to that of a single battery cell with inputs and outputs suitably scaled. While this approach requires the least computational effort, it is currently unclear how much loss in fidelity there is when not accounting for cell-to-cell heterogeneities. To the best of the author’s knowledge, no systematic comparison has been done between a battery pack model that explicitly captures the cell-to-cell heterogeneities and a simple scaled-up cell-level model using modularity has been done previously.

With the increasing availability of faster processors and specialized hardware such as GPUs, it is possible to model and predict battery pack dynamics by simulating the dynamics of all of the cells that comprise the battery pack. For example, the authors of [12] have simulated the electrical dynamics of a grid-integrated battery pack consisting of >21k cells, where each cell is modeled using a first-order equivalent-circuit model (ECM), as shown schematically in Fig. 1, with each cell’s parameters drawn from an empirically estimated distribution. This is done to account for cell-to-cell heterogeneity that arises during mass manufacturing. These simulations find that regions of the battery state-of-charge (SoC) that correspond to the highest variance in the parameter values also produces the greatest imbalance between the maximum and minimum measured cell voltages across the whole pack. In addition, the simulations also find that there is not a single dominant cell: the cell associated with the maximum (minimum) voltage changes throughout the simulation.

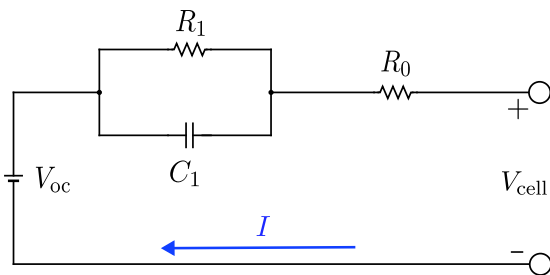


Fig. 1: Schematic representation of a first-order equivalent-circuit model (ECM). The electrical dynamics modeled using an RC loop mediated by a polarization resistance R_1 and polarization capacitance C_1 . The polarization timescale is then $\tau_1 = R_1 C_1$. Internal losses are modeled by a high-frequency resistance R_0 . We use the convention throughout that discharge corresponds to a positive current, $I > 0$.

To bridge the divide between cell-level and pack-level modeling, various studies have focused on understanding the dynamics of battery modules. The authors of [8] construct a model of a battery module’s dynamics which incorporates the battery’s electric, thermal, and aging dynamics. Similar

to [12], the authors model the electric dynamics of each cell within the module with an ECM model, where the parameters of the ECM are drawn from a Gaussian centered on a nominal value and with a variable variance. They also investigate the effects of cell balancing and examine the differences in the cell’s aging dynamics when using either passive or active balancing. The thermal dynamics of each cell is modeled using a lumped-parameter approach where the electrical dynamics generate heat and cells exchanges heat with each other through passive air cooling channels. The aging model used is based on severity factors and accounts for both capacity fade and resistance increase (or, equivalently, power fade) [9]. They find that, under similar load and conditions, the cells within a battery module ages faster relative to an isolated battery cell. Surprisingly, they find that the degree of cell-to-cell heterogeneity does not make an impact on this difference between pack-level aging and cell-level aging.

Yet another way to model the dynamics of a battery pack is to identify an ECM using battery pack data directly. In [13], a study was carried out to compare the performance of an ECM identified using the experimental data collected from a new Hyundai Kona 2019 vehicle. The experiment placed the car on a chassis dynamometer and it was driven to undergo a UDSS and US06 drive profile. During the experiment, pack-level and cell-level (from cells within the pack) electrical data were collected. The authors then did a performance comparison between two ECMs: one ECM is identified from the pack data directly, while another ECM is identified using the cell-level data and then scaled up to the pack-level using the modularity assumption. When the performance of the two models in predicting the pack-level experimental data is compared, as measured by the root-mean-square error of the model prediction with the data, it is found that both ECMs perform equally well in describing the battery pack’s electrical dynamics suggesting that the electrical dynamics can be adequately modeled by using the modularity assumption.

In this article, we aim to study the sensitivity of battery pack models to cell-to-cell heterogeneity. To accomplish this, we:

- 1) Build and calibrate a battery pack simulator wherein we model the dynamics of the individual cells in the pack by using an ECM for the electrical dynamics, a lumped-parameter model for the thermal dynamics, and a model of capacity fade and resistance increase based on discharge energy-throughput and severity factor
- 2) Study the effects of introducing capacity heterogeneities into the cells and the response of the cells and the pack overall to this heterogeneity
- 3) Investigate a mechanism by which the pack’s performance remains robust to the presence of heterogeneities

The model built in this work is inspired by one constructed in [8]; however, this study specifically focuses on drive cycles and loads relevant to battery EVs (BEVs) and also constitutes a larger pack than what was previously studied.

To calibrate and validate this model, we leverage experiments carried out at Idaho National Lab with data shared with us by the authors of [1]¹. The specifications of the cells and battery packs tested are listed in Tbl. I. Experiments were carried out over the period of one year and periodically tested the performance every month of a battery pack from a (first-generation) 2012 Nissan Leaf as it is subjected to a load representative of common EV operation. The design of the experiments from which we use the data are listed in Tbl. II. Data was collected both at the pack level and at the cell level (these cells are isolated and not part of the pack). The pack and cells for which data is used here were charged with a DCFC charging protocol at 120A. The experiment shows that a heterogeneous temperature distribution throughout the pack accelerates the aging of cells in the pack relative to that of isolated cells experiencing the same (appropriately scaled) load. We aim to construct a battery pack model that can recapitulate these experimental findings.

Battery specs	
Manufacturer	Nissan
Positive electrode	LiMn ₂ O ₄
Negative electrode	LiC ₆
Type	Prismatic
Nominal capacity [Ah]: cell/voltage	33.1/66.2
Nominal voltage [V]: cell/pack	3.8/362.5
Charge cutoff voltage [V]: cell/pack	4.1/787.2
Discharge cutoff voltage [V]: cell/pack	2.5/480
Total number of cells in pack	192
Module configuration	2p2s

TABLE I: Specifications for battery pack and isolated cells used in the experiments of [1].

Using the pack model, We investigate how the dynamics of a pack containing cells whose capacity is drawn from a known distribution differs from a pack which contains only cells with nominal capacity. We compare our the results of our pack simulator with cell-to-cell heterogeneity to a pack model that assumes modularity and quantify the differences between the predictions of these two models. In so doing, we investigate the validity of using the modularity assumption when modeling battery packs. We then investigate how initial cell-to-cell heterogeneities propagate in time at the level of the electrical and thermal response of the battery pack. Specifically, we investigate how the presence of “weak” cells with a known lowered capacity in the pack affect the

¹In this work, we use data based on the cells aged using DC fast charging; however, as seen in [1, Fig. 3], the difference in aging between the two charging levels at the cell-level is marginal.

V_{\max}/V_{\min} [V]	Temperature [°C]	Number of Packs or cells	Capacity at BOL [Ah]
Pack			
395/285	30	1	56.34
Cell			
4.11/2.5	20	3	28.30 ± 0.05
	30	3	28.24 ± 0.05
	40	3	28.28 ± 0.08

TABLE II: Design of experiments for cell and pack data that is used in this work from [1].

dynamics of cells in the pack that are “normal” and have nominal capacity.

The remainder of the article is organized as follows: In Sec. gives an overview of the individual battery cell model which integrates the electrical (Sec. II-A), thermal (II-B), and aging (II-C) dynamics. In Sec. II-D we explain how the cell model is identified. Having an identified battery cell model, we lay out in Sec. II-E how these cell models can be interconnected to form a battery pack which we use to investigate the effect of cell-to-cell heterogeneity on the pack outputs in Sec. III. Specifically, in Sec. III-B we present the sensitivity of the pack electrical quantities given a certain level of capacity heterogeneity; Sec. III-D presents an analysis of a mechanism by which the robustness of the pack voltage quantities can be explained.

II. METHODS

In this section, we outline the models used to describe the dynamics of an individual cell. Figure 2 shows the interactions of the different components of the model. We explain how these cell-level models are identified and subsequently interconnected to form a model for the battery pack.

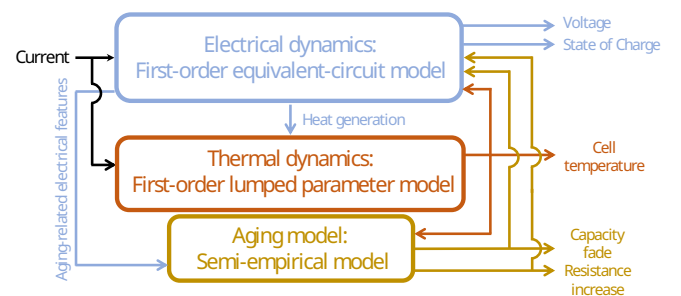


Fig. 2: Schematic showing how the connections between the electrical, thermal, and aging dynamics. The primary output of the electrical model is the voltage and the state-of charge. The thermal model outputs the cell temperature which is affected by internal losses in battery during operation, as well as the heat exchange with the ambient temperature and any surrounding cells. The aging model takes in the aging-related features (energy-throughput, state-of-charge, and temperature) and predicts the capacity fade and resistance increase which has a feedback on the electrical model.

A. Cell-level electrical model

We model the cell-level electrical dynamics using a first-order ECM as shown in Fig. 1. Given this model, the

dynamical equations for the internal states of the i th battery cell are [14],

$$\frac{d}{dt} \text{SoC}^{(i)}(t) = -\frac{1}{3600 \cdot Q^{(i)}} I^{(i)}(t), \quad (1a)$$

$$\frac{d}{dt} V_{\text{RC}}^{(i)}(t) = -\frac{1}{\tau_1^{(i)}} V_{\text{RC}}^{(i)}(t) + \frac{1}{C_1^{(i)}} I^{(i)}(t). \quad (1b)$$

Equation (1a) tracks the SoC of the cell through Coulomb counting, while (1b) determines the dynamics of polarization voltage $V_{\text{RC}}^{(i)}$ given a the polarization timescale τ_1 and the polarization capacitance C_1 . The capacity of the cell (measured in units of Ampere-hour) is denoted by $Q^{(i)}$. The battery-cell terminal voltage is determined by,

$$V_{\text{cell}}^{(i)}(t) = V_{\text{oc}}(\text{SoC}^{(i)}) - V_{\text{RC}}^{(i)}(t) - I^{(i)}(t) R_0(\text{SoC}^{(i)}, T_{\text{cell}}^{(i)}), \quad (2)$$

where $V_{\text{oc}}(\text{SoC}^{(i)})$ represents an empirical relationship between the open-circuit voltage (OCV) and SoC which is estimated from $C/3$ discharge capacity test data (Fig. 15) and $R_0(\text{SoC}^{(i)}, T_{\text{cell}}^{(i)})$ is the high-frequency resistance. Throughout this article, we use the convention that positive current $I^{(i)} > 0$ corresponds to discharge of the battery. This model is chosen as it is sufficiently detailed to be able to capture the battery dynamics while still being relatively computationally cheap to allowing for many electrical interconnections.

B. Cell-level thermal model

To model the cell's thermal dynamics we assume a one-state lumped parameter thermal model [15],

$$C_{\text{cell}} \frac{d}{dt} T_{\text{cell}}^{(i)}(t) = I_{\text{cell}}(t) [V_{\text{oc}}(\text{SoC}^{(i)}) - V_{\text{cell}}^{(i)}(t)] + \frac{1}{R_c} [T_{\text{amb}}(t) - T_{\text{cell}}^{(i)}(t)] + \frac{1}{R_c} [T_{\text{cell}}^{(i-1)}(t) - T_{\text{cell}}^{(i)}(t)] + \frac{1}{R_c} [T_{\text{cell}}^{(i+1)}(t) - T_{\text{cell}}^{(i)}(t)]. \quad (3)$$

Here, C_{cell} denotes the cell's heat capacity, R_c denotes the conductive resistance the cell and the housing, and T_{amb} denotes the ambient temperature. The first term on the right-hand-side of (3) models the losses associated with the high-frequency resistance and polarization dynamics. The last two terms denote the contribution to the cell's temperature of any interconnections between adjacent cells.

C. Cell-level aging model

To model capacity-fade of the battery cells, we construct a semi-empirical model of the capacity fade based on discharge energy-throughput,

$$\text{Wh}_{\text{disch}}^{(i)}(t) = \frac{1}{3600} \int_0^t ds \Theta[I^{(i)}] I^{(i)}(s) V^{(i)}(s), \quad (4)$$

and temperature-dependent severity factor $\sigma_Q(T)$:

$$Q_{\text{loss}}^{(i)}(\text{Wh}_{\text{disch}}^{(i)}) = \sigma_Q(T) [\text{Wh}_{\text{disch}}^{(i)}]^{1/2}. \quad (5)$$

In (4), $\Theta[\cdot]$ denotes the Heaviside function which enforces that only discharge events contribute to the energy-throughput.

The choice of using discharge energy throughput is motivated by the experimental data available although it differs from previous works, (e.g. [8], [9]) where aging models are based on ampere-hour throughput. Nevertheless, it suffices to empirically characterize the capacity fade and resistance increase observed.

The value of the exponent in (5) is fixed to 1/2, motivated by previous work [9], which we retain since this results in a good fit to the experimental data (see Fig. 3a). The severity factor is dependent on temperature which we model as an Arrhenius factor,

$$\sigma_Q(T) = \gamma_Q \exp\left(-\frac{\alpha_Q}{T}\right). \quad (6)$$

Capacity fade data is obtained from $C/3$ capacity tests performed at every month the experiment was run. The identified coefficients were obtained from least-squares fitting of the obtained severity factor values (Fig. 3b) and are listed in Tbl. V.

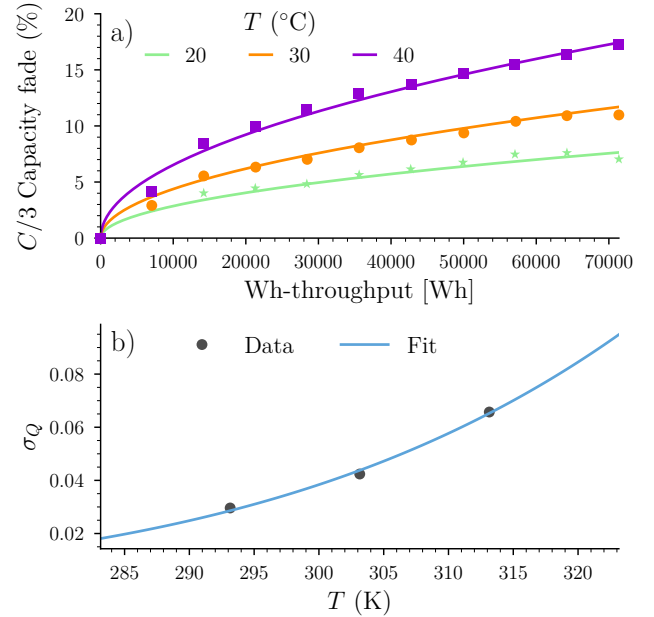


Fig. 3: **Capacity fade aging model fits to data.** a) Capacity fade based on $C/3$ capacity test. Points denote experimental data, obtained from [1, Fig. 3]. Solid lines show the predictions of the semi-empirical capacity fade model (5). Different colors denote data for different temperatures. b) Severity factor (6) (blue solid curve) fit to the obtained values of the severity factor (black points) as a function of temperature.

We model the resistance increase of the battery cells using a similar a semi-empirical model of the form,

$$R_{0,\text{incr}}^{(i)}(\text{Wh}_{\text{disch}}^{(i)}) = \sigma_{R_0}(\text{SoC}, T) [\text{Wh}_{\text{disch}}^{(i)}]^{1.05}, \quad (7)$$

where the severity factor is a function of SoC and T :

$$\sigma_{R_0}(\text{SoC}, T) = \left| \sum_{j=0}^4 \theta_{1j} \cdot (\text{SoC})^j \right| \times \exp \left(\sum_{k=0}^4 \theta_{2k} \cdot (\text{SoC})^k \right) \exp \left(-\frac{\alpha_{R_0}}{T} \right). \quad (8)$$

The exponent in (7) and the coefficients in (8) are obtained from least-squares fitting to HFR increase values obtained by calibrating an ECM model to HPPC data obtained at different months of the experiment (see App. V for more details). The values of the coefficients θ_{ij} and α_{R_0} of the model are listed in Tbl. VI. The severity factor (8) is shown in Fig. 4 as a function of SoC and temperature.

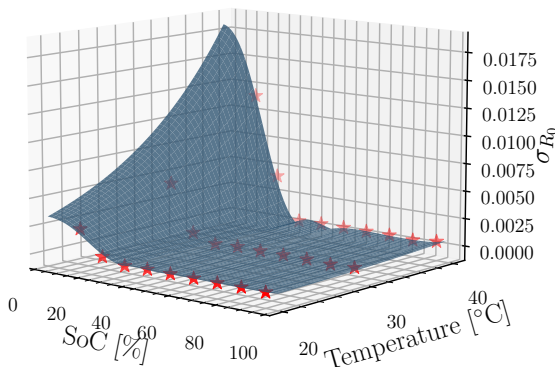


Fig. 4: **Resistance increase severity factor.** Severity factor as a function of SoC and temperature. The surface is parameterized by (8) with the parameters inferred by fitting to the severity function values (stars). The coefficient values corresponding to the surface shown are listed in Tbl. VI.

D. Cell-level model calibration

To calibrate the battery cell electric and thermal models we use experimental hybrid-pulse power characterization (HPPC) data from [1] to find a set of parameters θ^* that minimizes the root-mean-square percent error (RMSPE),

$$\theta^* = \arg \min_{\theta} \text{RMSPE}(\theta) \quad (9)$$

between the model's prediction of the value of an observable \mathcal{O}_i and its experimentally measured value,

$$\text{RMSPE}(\theta) = 100 \sqrt{\frac{1}{N_{\text{meas}}} \sum_{k=1}^{N_{\text{meas}}} \left(1 - \frac{\mathcal{O}_i^{\text{model}}[k; \theta]}{\mathcal{O}_i^{\text{exp}}[k; \theta]} \right)^2}, \quad (10)$$

where N_{meas} is the total number of measurements. The index i distinguishes between different observables of the model.

To calibrate the electrical model, we consider as the set

of parameters,

$$\theta_{\text{electric, cell}} = (R_0 \quad \tau_1 \quad C_1), \quad (11)$$

and the corresponding observable is the cell terminal voltage $\mathcal{O}_{\text{electric, cell}} = V_{\text{cell}}$. We identify the parameters of the electric model for every 10% SoC increment. Similarly, to calibrate the thermal model, we consider the parameters,

$$\theta_{\text{thermal, cell}} = (C_{\text{cell}} \quad R_c), \quad (12)$$

with the corresponding observable being the cell temperature $\mathcal{O}_{\text{thermal, cell}} = T_{\text{cell}}$.

The results for the cell and pack model calibrations using the procedure detailed above are shown in Sec. III-A.

E. Battery pack model

Having identified and integrated the cell-level electric, thermal, and aging dynamics, we construct a cell-level battery pack model by connecting cells in the configuration corresponding to the Nissan Leaf battery pack [1]. The battery pack is made of 48 modules connected in series, where each module has cells in a 2p2s configuration resulting in 192 cells in total. All cells, and all modules, within the battery pack exchange heat via convection. The model is implemented in MATLAB Simulink/Simscape. For each of the cells in the pack, a timeseries of current, voltage, temperature, SoC, capacity, and high-frequency resistance value are collected.

III. RESULTS

A. Cell and pack model identification

We identify the cell electrical model using the procedure outlined in Sec. II-D. The parameters identified as a function of SoC are shown in Fig. 5. These parameters are obtained from averaging the results of identification for each of the three cells tested at each temperature condition. The standard deviation of the parameters identified from the three cells, averaged over SoC, are shown in Tbl III

Temperature ($^{\circ}\text{C}$)	20	30	40
Σ_{R_0} (m Ω)	0.067	0.012	0.12
Σ_{τ_1} (s)	2.17	1.19	1.32
Σ_{C_1} (F)	327.71	367.54	523.47

TABLE III: Standard deviation Σ_i of identified parameters as a function of temperature. All standard deviations have been averaged over SoC.

We find that only the internal resistance R_0 has a significant dependence on the temperature T (see App. I). The dynamical parameters, the polarization timescale τ_1 and the polarization capacitance C_1 , are not strongly dependent on (Fig. 14) temperature. As such, we also average the estimates for τ_1 and C_1 obtained from the calibration over the different temperatures.

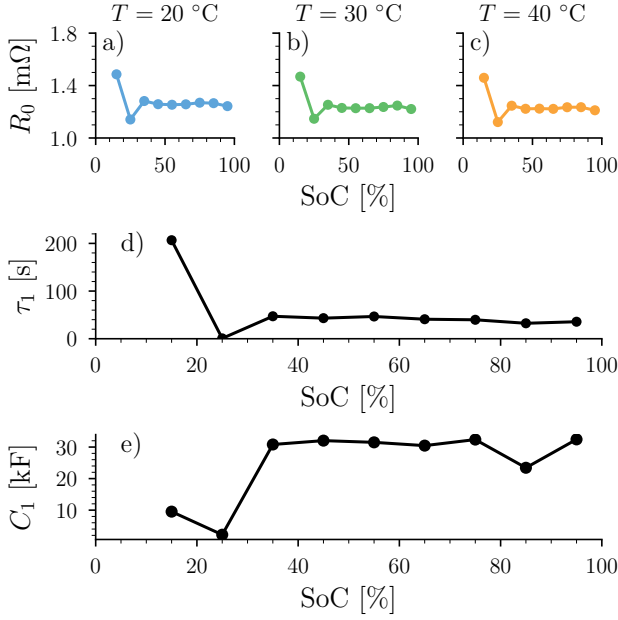


Fig. 5: Identified first-order cell ECM parameters as a function of SoC. a-c) Internal resistance R_0 at different temperatures. (d) Polarization timescale τ_1 . (e) Polarization capacity C_1 .

Applying a standard hybrid-pulse power characterization (HPPC) profile to the identified model, we compare the model output to the experimentally measured voltage and temperature in Fig. 6. To give a quantification of the magnitude of the error, along with the RMSPE, we also report the root-mean-square error (RMSE),

$$\text{RMSE}(\theta) = \sqrt{\frac{1}{N_{\text{meas}}} \sum_{k=1}^{N_{\text{meas}}} (\mathcal{O}_i^{\text{exp}}[k; \theta] - \mathcal{O}_i^{\text{model}}[k; \theta])^2}, \quad (13)$$

between the experimentally measured observables and the model predictions. We observe excellent agreement between the identified model and the experimental data with an RMSPE of 3% and 0.24% for the voltage and temperature, respectively. The agreement between the calibrated electrical model and the experimental data is noticeably poorer at low SoCs. This is likely caused by the inaccuracy of the pseudo-OCV vs. SoC relationship, $V_{\text{oc}}(\text{SoC}^{(i)})$ in (2), due to the relationship being estimated using a C-rate of $C/3$ as opposed to a lower current rate such as $C/20$ (see App. III for pseudo-OCV plot and further discussion). The current rate used in the capacity test induces a higher overpotential leading to discrepancies between the pseudo-OCV and the true OCV particularly at low SoCs.

Once the electric model is identified, we then identify the thermal parameters. The identified parameters are listed in Tbl. IV

We validate the identified model by using a dynamic stress test (DST) profile. Applying the same profile to the identified model, we find excellent agreement in both voltage and temperature between the experimental data and the identified

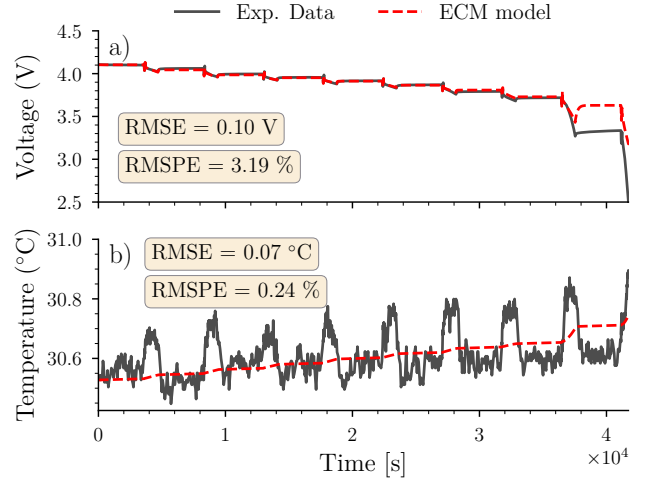


Fig. 6: The electrical and thermal model parameters are identified using experimental HPPC data. a) Voltage comparison between experimental data (black solid curve) and model prediction (dashed red curve). b) Temperature comparison between data and model. The ambient condition for the HPPC data shown is $T_{\text{amb}} = 30\text{ °C}$.

Parameter	Value
C_{cell} (kJ/K)	27.5
R_{cell} (K/W)	38.46

TABLE IV: Thermal model parameters.

model in Fig. 7. We show a more complete validation of the identified single-cell model across a variety of temperature and aging conditions in the appendix (Figs. 16 & 17).

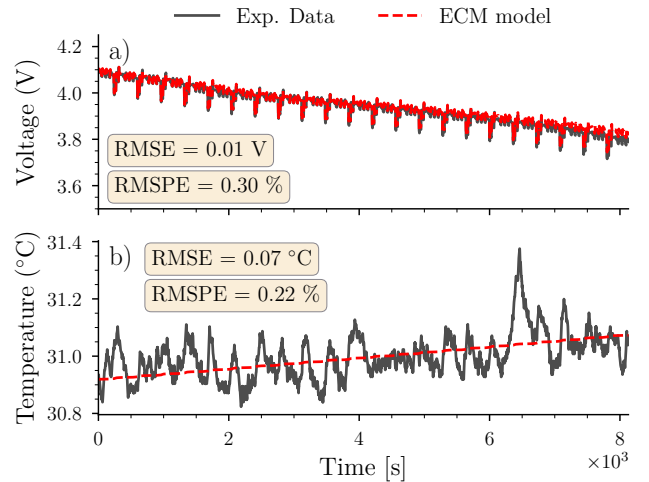


Fig. 7: The DST experimental data is used to validate the single battery cell model. a) Voltage comparison between experimental data (black solid curve) and model prediction (red dashed curve). b) Temperature comparison. The ambient temperature is set to $T_{\text{amb}} = 30\text{ °C}$

We construct a battery pack model (see Sec. II-E), as-

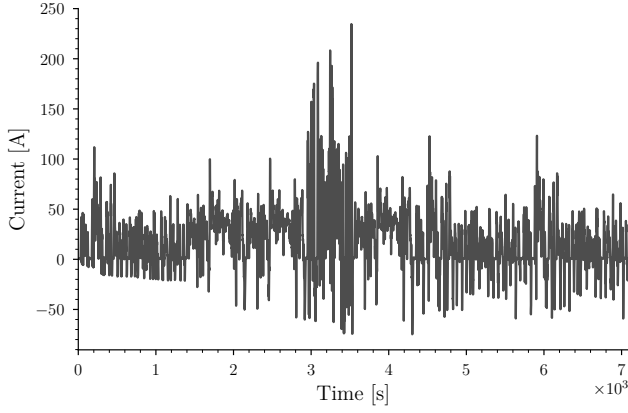


Fig. 8: *Dynamic input current profile based on Nissan Leaf data used in battery pack simulations.*

suming that the pack contains no heterogeneities given an input of the dynamic current profile Fig. 8, and compare the model output to experimental data in Fig. 9. We find that the homogeneous battery pack model output agrees well with the experimental data with a low voltage RMSPE of 0.41%. The experimental temperature battery pack data shows large amounts of discretization of 1°C thus making it unreliable for comparison. Thus, we omit a direct comparison of the battery pack temperature.

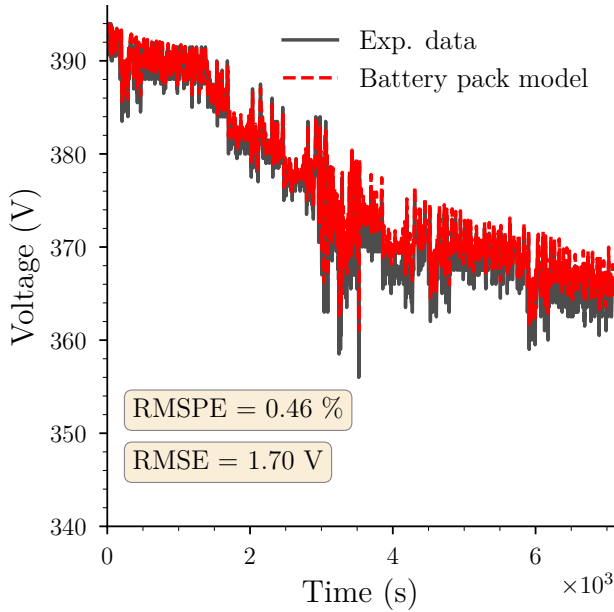


Fig. 9: *The experimental battery pack data validates the constructed pack model. Experimental measurements under the dynamic current profile (Fig. 8) (solid black curve) is compared against the model output voltage from the identified battery pack model (dashed red curve).*

B. Effect of having a distribution of initial capacities

Having validated the model, we now investigate the effect of introducing heterogeneities. As we are tracking the dynamics of each cell, we can incorporate heterogeneities

explicitly. We particularly focus on the effects on the pack's output if the initial capacity of each cell in the pack is drawn from a normal distribution,

$$Q^{(i)}(t=0) \sim \mathcal{N}\left(Q^{(i)}; \mu = Q_{\text{nom}}, \Sigma_Q^{\text{initial}}\right), \quad (14)$$

whose mean is fixed at the nominal capacity of the cells $Q_{\text{nom}} = 33.1$ Ah and with a variable standard deviation $\Sigma_Q^{\text{initial}}$.

In Fig. 10, we observe the effects of the introduction of a specific level of capacity heterogeneity (14) $\Sigma_Q^{\text{initial}}$ on the distribution of capacity, SoC, and the high-frequency resistance R_0 , after applying the dynamic current profile shown in Fig. 8. We observe (Fig. 10a) that the final distribution of cell capacities has a standard deviation very similar to that of the initial distribution, $\Sigma_Q^{\text{final}} \approx \Sigma_Q^{\text{initial}}$ indicating that, while the capacity of all the cells in the pack decreases due to usage, the spread in the capacity distribution does not change appreciably over the application of a single cycle.

Introduction of capacity heterogeneity invariably introduces a heterogeneity in the SoC of the cells in the pack since SoC depends on the capacity (1a). For simplicity, we assume that the SoC of all the cells in the pack, prior to the application of the dynamic current profile, are the same: $\text{SoC}^{(i)}(t=0) = 95\% \forall i$. After the application of the current profile, we see (Fig. 10b) that the standard deviation of the distribution of the SoCs $\Sigma_{\text{SoC}}^{\text{final}}$, follows a similar trend to that of the standard deviation of the capacities, $\Sigma_{\text{SoC}}^{\text{final}} \approx \Sigma_Q^{\text{final}}$, suggesting that the heterogeneity in cell's capacity propagates to the cell SoCs.

This distribution of SoC values also affects the electric parameters. Specifically, we focus our attention on its effect on the high-frequency resistance R_0 (HFR) as it has previously been identified to be the parameter that the ECM model is most sensitive to [16]. A similar analysis could also be done for the other electric parameters. Since we assume that all the SoCs of the cells are the same before application of the current profile then all cells also have the same resistance value (i.e. there is no spread in initial HFR values). We observe (Fig. 10c) that, after applying the dynamic drive cycle profile, the distribution of SoC values also results in the cells of the pack having a distribution of HFR values with a standard deviation $\Sigma_{R_0}^{\text{final}}$ that grows monotonically with the initial capacity standard deviation. However, the heterogeneity introduced in the SoC and the HFR, as measured by the standard deviation, is much less than the heterogeneity that is introduced into the capacity initially, $\Sigma_{R_0}^{\text{final}} \ll \Sigma_Q^{\text{initial}}$.

C. Comparison of cell-level battery pack model and a simple pack model based on modularity assumption

Having seen that the introduction of capacity heterogeneity indirectly also introduces heterogeneities in various electric model parameters, we now investigate the effect of this heterogeneity on the inferred battery pack voltage and temperature. To do this, we compute the difference between the

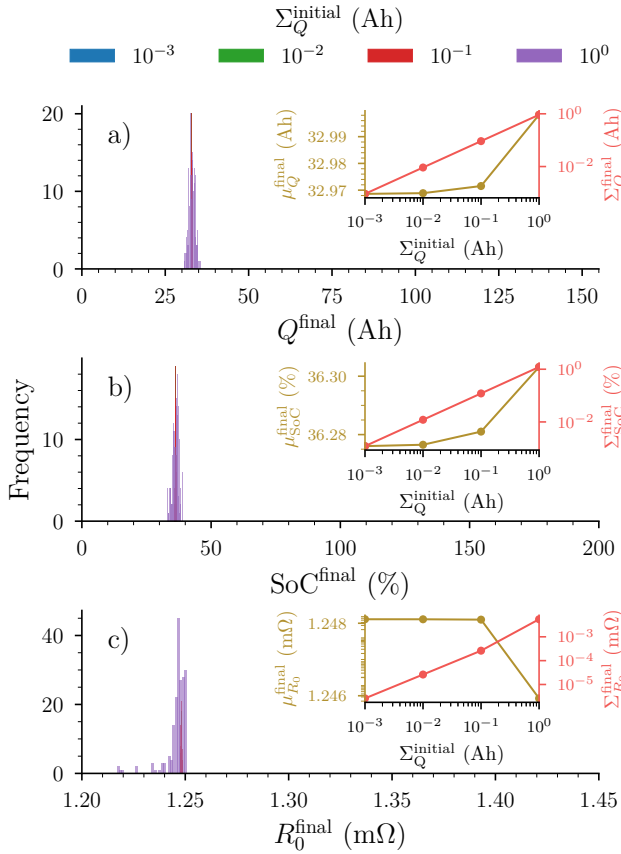


Fig. 10: Introduction of capacity heterogeneity in the form of (14), introduces heterogeneity to the SoC and the internal resistance. Each plot shows the distribution of cell quantities after the application of the input shown in Fig. 8 for different values of the initial capacity standard deviation $\Sigma_Q^{\text{initial}}$. a) Distribution of capacities Q^{final} of all the cells in the pack. b) Distribution of state-of-charge $\text{SoC}^{\text{final}}$ of all the cells in the pack. c) Distribution of high-frequency resistance R_0^{final} of all the cells in the pack. Insets show the mean (left axis) and the standard deviation (right axis) for each of the distributions shown as a function of the initial capacity standard deviation.

voltage and temperature signals

$$\Delta V_{\text{pack}}(t) = V_{\text{pack}}^{\text{het}}(t) - V_{\text{pack}}^{\text{nom}}(t) \quad (15a)$$

$$\Delta T_{\text{pack}}(t) = T_{\text{pack}}^{\text{het}}(t) - T_{\text{pack}}^{\text{nom}}(t), \quad (15b)$$

between a pack that has capacity heterogeneities, denoted by the superscript “het”, and one to one that does not (i.e., all cells have the same nominal capacity), denoted by “nom”.

In Fig. 11, we see that the introduction of capacity heterogeneity introduces small differences in the pack’s voltage and temperature; however, we note that such deviations are relatively small suggesting that the predictions of a pack explicitly modeling cell-to-cell heterogeneity would be indistinguishable to the predictions of a pack without heterogeneities for a single cycle unless the introduced heterogeneities are particularly severe. The introduction of capacity heterogeneities does result in an increase in the spread of temperature values experienced by the cells of the pack throughout the cycle (Fig. 11b). This inhomogeneity of temperatures would likely be exacerbated upon repeated use

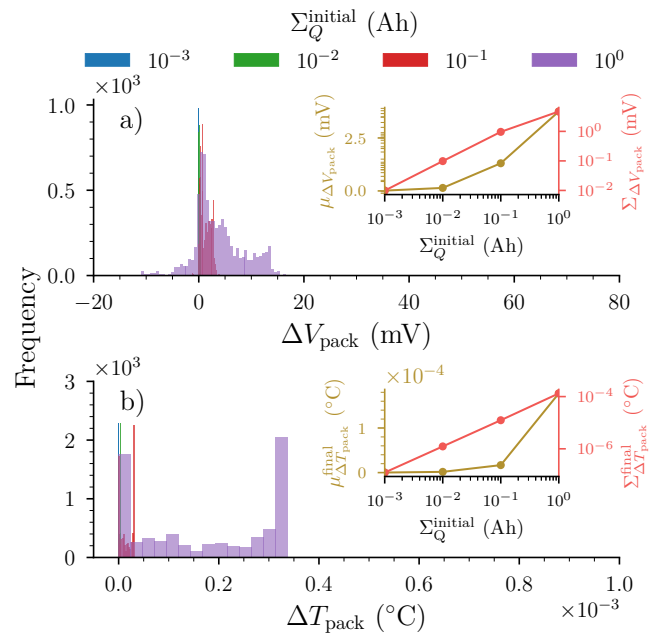


Fig. 11: Introduction of capacity heterogeneity in the form of (14), introduces small differences in the voltage and temperature of the pack. Each plot shows a pack-level quantity after the application of the input shown in Fig. 8 for different values of the initial capacity standard deviation $\Sigma_Q^{\text{initial}}$. a) Distribution of differences in pack voltage between a pack with capacity heterogeneity and without (15a). b) Distribution of differences in pack temperatures between a pack with capacity heterogeneity and without (15b). Insets show the mean (left axis) and the standard deviation (right axis) for each of the distributions shown as a function of the initial capacity standard deviation.

of the battery resulting in an acceleration of aging.

D. Effect of lower capacity cells in the pack

We investigate the effects of heterogeneity in the battery pack by introducing cells of lower capacity into the battery pack. Specifically, we pick uniformly randomly from the 192 total cells in the pack N_{weak} cells to be “weak”: We replace the chosen N_{weak} cells in the pack with cells that are equivalent in all parameters but with capacities lowered by a percentage p . Figure 12 shows the effect of this heterogeneity on the pack output energy. In particular, it shows the reduction of the energy delivered by the pack during the application of the input current profile in the presence of weak cells. We observe that for $N_{\text{weak}} < 30$, or equivalently when $< 20\%$ of the cells in the pack are weak, the percentage decrease of energy delivered relative to when all of the cells in the pack are nominal is small $\ll 1\%$. The percentage decrease of energy delivered increases monotonically when the number of weak cells or the percent of capacity reduced is increased. Only when 77 weak cells in the pack, corresponding to 40% of the total number of cells, and for the largest percent reduction in capacity per cell of 40% that we consider, do we see that the percent decrease in energy delivered becomes $> 1.5\%$. Thus, unless heterogeneity is very high, the effects of capacity heterogeneity on the output pack energy is low.

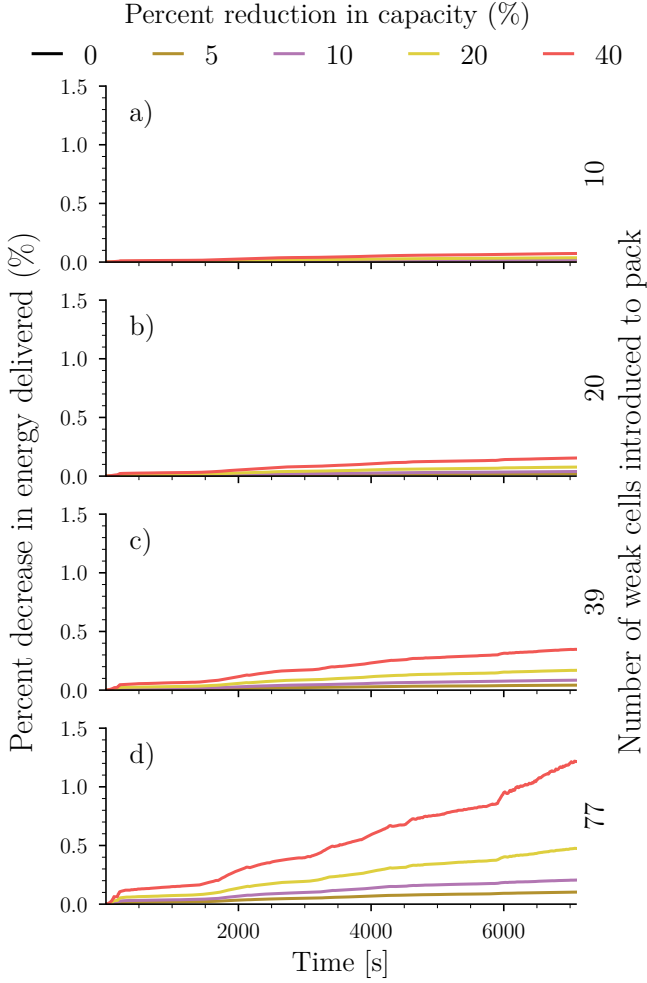


Fig. 12: A large number of weak cells must be introduced in order to have a significant effect the energy delivered by the battery pack. Each plot shows the percent decrease in energy delivered of a pack with weak cells compared to a pack where all cells are nominal as a function of time for the input shown in Fig. 8. The number of weak cells introduced to the pack increases going down the rows (a-d). Different colors within a given subplot denote different percent of capacity reduction from the nominal capacity of the introduced cells.

To explore how heterogeneities affect the cells in the battery pack, we examine the final SoC values obtained by the cells in the battery pack. Specifically, we focus on the 20 cells (five modules) that are closest electrically to the negative terminal of the pack for ease of presentation; however, the behaviors seen in these modules are representative of the other modules in the pack. We show, in Fig. 13a, the final SoC values obtained by these cells in the pack after applying the dynamic current profile shown in Fig. 8 when 77 weak cells with 40% capacity reduction relative to their nominal capacity are introduced to the battery pack in place of cells with nominal capacity. This is an extreme case of capacity heterogeneity but more clearly illustrates the effects of these weaker cells on their neighbors.

We observe that pairs of cells within a parallel branch fall into one of three distinct types (Fig 13a): (1) both cells

within a parallel branch are normal, (2) both cells within a parallel branch are weak, and (3) only one of the cells within a parallel branch is weak. When both cells within a parallel branch have nominal capacities, then they obtain the same final SoC as if there were no weak cells introduced into the pack. Conversely, when both of the cells in the parallel branch are weak, they are completely drained of charge after application of the input current profile. When only one of the cells in a parallel branch is weak, we see that both cells within the branch achieve an intermediate value of SoC relative to branches from the first two cases.

To understand why cells in a parallel branch of type (3) obtain an intermediate value of final SoC, we compute the difference between the total energy-throughput,

$$\text{Wh}^{(i)}(t) = \frac{1}{3600} \int_0^t ds I_{\text{cell}}^{(i)}(s) V_{\text{cell}}^{(i)}(s), \quad (16)$$

of the cells $i \in \{1, 2, \dots, 192\}$ in battery pack with weak cells, $\text{Wh}_{\text{weak}}^{(i)}$, to the energy-throughput of the cells in a battery pack without weak cells $\text{Wh}_{\text{nom}}^{(i)}$:

$$\Delta \text{Wh}^{(i)} = \text{Wh}_{\text{weak}}^{(i)} - \text{Wh}_{\text{nom}}^{(i)}. \quad (17)$$

We see in Fig. 13b that for parallel branches where one of the cells is weak (e.g. see cells 1 & 2), the stronger of the two cells takes on a greater amount of energy-throughput than it otherwise would if both of the cells in the branch were at nominal capacity. In this particular case, the stronger cell discharges 15 Wh more energy compared to the nominal case; in contrast, the weaker cell discharges 19 Wh less energy. This accommodation of the weaker cells by the stronger cells may explain why the effect on the output energy of the battery pack is relatively small until the level of heterogeneity in the pack is sufficiently large: Only when there are sufficiently many pairs of cells that are both weak will the voltage output of the pack suffer.

While this accommodation or “balancing” effect is beneficial, in that the effect of heterogeneity on the short-term pack output energy is small, long-term it can be overall detrimental to the cells in the pack as bearing higher loads generally also implies a greater amount of aging. To quantify this, we use the cell-level aging models to compute the difference,

$$\Delta Q_{\text{loss}}^{(i)} = Q_{\text{loss,weak}}^{(i)} - Q_{\text{loss,nom}}^{(i)}, \quad (18)$$

between the fraction of capacity remaining in the cells of the pack with weak cells,

$$Q_{\text{loss,weak}}^{(i)} = \frac{Q_{\text{initial,weak}}^{(i)} - Q_{\text{final,weak}}^{(i)}}{Q_{\text{initial,weak}}^{(i)}} \quad (19)$$

to the fraction of capacity remaining in the cells of the pack without weak cells

$$Q_{\text{loss,nom}}^{(i)} = \frac{Q_{\text{initial,nom}}^{(i)} - Q_{\text{final,nom}}^{(i)}}{Q_{\text{initial,nom}}^{(i)}}. \quad (20)$$

A positive value of (18) implies a greater amount of aging for a given cell i in a pack with weak cells, relative to the amount

of aging it would have experienced if all of the cells had nominal capacity. We see (Fig. 13c) that the cells which bear a higher energy-throughput due to having a weak partners experience a significant amount of aging relative to what they would have if all the cells in the pack were at nominal capacity.

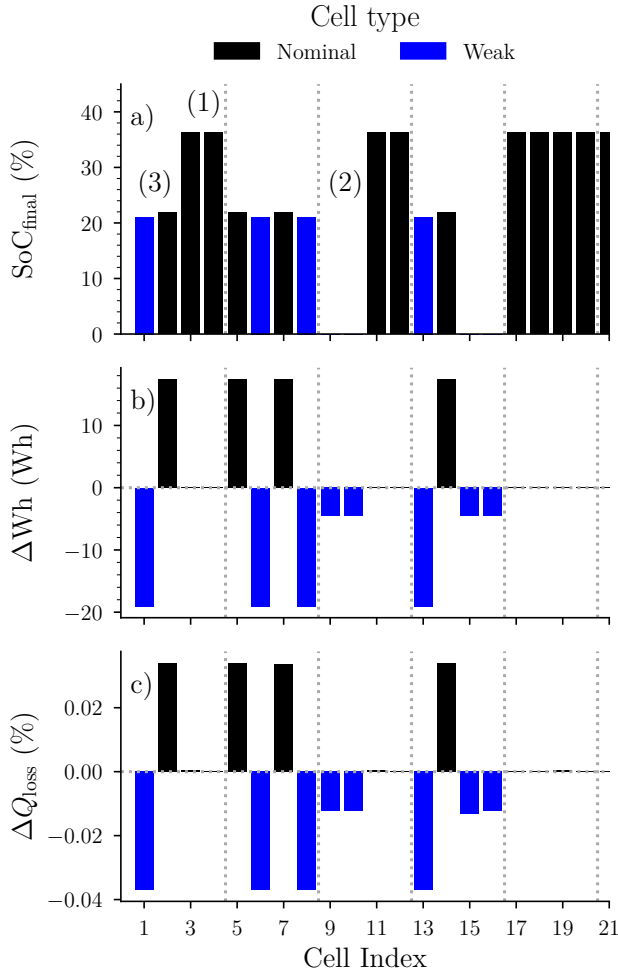


Fig. 13: **Stronger cells can accommodate for weaker cells at the expense of increased aging.** a) The SoC of the first 20 cells (five modules) in the pack. The three distinct types of parallel branches, or pair of cells, are distinguished by (1) both normal, (2) both weak, and (3) one weak and one normal. b) The difference of energy-throughput between cells in a pack with weak cells and cells in a pack without weak cells. c) The difference in capacity aging between the cells in a pack with weak cells and cells in a pack without weak cells. Cells that are weak have reduced capacity and are shown in blue, while cells with nominal capacity are shown in black. The gray dashed vertical lines demarcate which cells are grouped together in a single module with a 2p2s (4 cells/module) configuration. Subsequent numbers are paired together in a parallel branch.

IV. CONCLUSIONS

In this article, we have constructed a battery pack model to investigate the effects of cell-to-cell heterogeneity. We use experimental data to calibrate and validate the models, both at cell and pack level. For sake of generality, we have not specified the source of the initial cell-to-cell heterogeneity that is introduced into our models. Heterogeneity in the cells

of a battery pack generally arise due to small variations during cell mass manufacturing or due to inhomogeneous aging of cells in the pack throughout its lifetime. Regardless of its source, we examine here the effect a certain level of heterogeneity has on the outputs of the pack model.

Using the pack model, we examined the effect of capacity heterogeneity that originate from a distribution. Capacity heterogeneities result in the heterogeneity of SoC, which then result in heterogeneity of other electrical quantities, particularly the high-frequency resistance. Despite these heterogeneities, we observe that, unless the heterogeneity is particularly severe, within a single application of a dynamic drive cycle, the effect of these heterogeneities on the pack voltage and temperature are small. As such, for a sufficiently low amount of cell-to-cell variability, a model of a battery pack upscaled from a single cell using modularity assumptions (i.e. neglecting cell-to-cell variability) gives a good approximation to the battery pack voltage and thermal dynamics.

In addition, we have observed that the presence of “weak” cells with reduced charge capacity in the pack, can be accommodated for by “stronger” cells with relatively higher load. Due to this, the battery pack can accommodate a relatively large amount of cell-to-cell heterogeneity without affecting the pack’s output voltage. This increase in load (current) borne by the stronger cells increases the rate of aging for these cells in a given cycle. As such, the “balancing effect” of cells in parallel comes at the cost of increased aging for the stronger cells in the pack.

ACKNOWLEDGEMENT

The authors thank the members of the Stanford Energy Control Lab for helpful discussions and feedback on the manuscript. Experimental data used in this work was provided by Dr. Eric Dufek and Mr. Matthew Shirk (Idaho National Lab). This work is part of Lab Call Project L096-1568 done in partnership with The Ohio State University and Oak Ridge National Lab. J.N.E.L. gratefully recognizes additional support from the National Sciences and Engineering Research Council of Canada (PGS-D). Funding for this project is provided by the Vehicles Technologies Office (VTO). This research is enabled in part through computational resources and support provided by Sherlock compute cluster @ Stanford University (<https://www.sherlock.stanford.edu>)

APPENDIX I

PARAMETER VARIATION AS A FUNCTION OF TEMPERATURE

We show the full set of identified parameters from each cell tested at the beginning of life as a function of SoC and temperature in Fig. 14. The voltage sense leads for cells 1 and 2 had higher internal resistance values for the first 3 reference performance tests (RPTs) [17]. As such we only use the data/parameters from cell 3 for the first 3 RPTs in all our analysis involving aging.

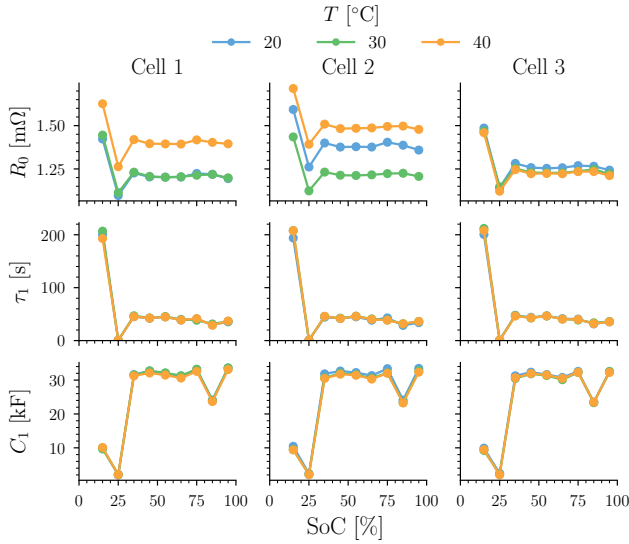


Fig. 14: Identified parameters for fresh cells as a function of SoC and temperature for the three cells within the dataset. The three ECM parameters are shown in the rows. Identified electrical parameters for different cells are shown in the different columns. Different colors denote different ambient temperature conditions.

APPENDIX II

AGING MODELS - SEVERITY FACTORS

The table of identified coefficients for the capacity fade severity factor (6) is listed in Tbl. V.

Parameter	Value
α_Q (K)	3.78782×10^3
γ_Q	1.16872×10^4

TABLE V: List of coefficient values that define the severity factor for the capacity fade model (5).

The table of identified coefficients for the resistance increase severity factor (8) is listed in Tbl. VI.

i	0	1	2	3	4
θ_{1i} ($\times 10^{-2}$)	1.56	-6.144	1.763	6.926	3.533
θ_{2i}	25.51	3.67	-4.57	-32.72	28.85
α_{R_0} (K)	7994				

TABLE VI: List of coefficient values that define the severity factor for the resistance increase model (8).

APPENDIX III

COMPARISON OF PSEUDO-OPEN CIRCUIT VOLTAGE OBTAINED FROM TWO DIFFERENT METHODS

We compare the pseudo-open circuit voltage (pseudo-OCV) obtained from a C/3 static capacity test done on an individual isolated cell to the pseudo-OCV obtained by measuring the voltage of the battery at the end points of the one-hour rest period of the HPPC test (Fig. 6a, black curve).

Figure 15 shows that the pseudo-OCV curves obtained from these two methods. We observe that there is good agreement between the two methods at SoCs $> 25\%$; however, below this value we see a marked difference between the pseudo-OCV and the OCV obtained from the HPPC. The polarization effects at low SoCs for the pseudo-OCV is particularly high likely leading to the discrepancy at low SoC values that we observe in Fig. 6a.

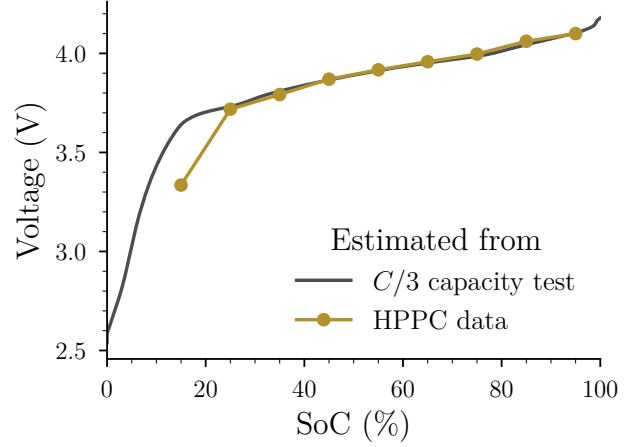


Fig. 15: A comparison between the pseudo-open circuit voltage (pseudo-OCV) obtained from a C/3 capacity test of an individual isolated cell at the beginning of life and the pseudo-OCV inferred from an HPPC test done on the same cell.

APPENDIX IV

CELL VALIDATION RESULTS

We show the validation results for our single-cell model across a variety of ambient temperature conditions and reference performance tests (aging) in Fig. 16.

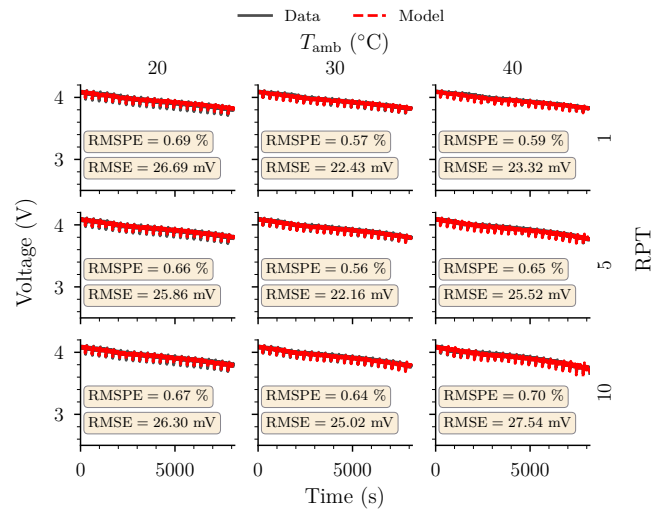


Fig. 16: We use the experimental voltage data to validate the electrical part of the single battery-cell model across a wide range of conditions. Every subplot shows the experimental (solid dark curve) and the model (dashed red curve) voltage as a function of time. Variation of ambient conditions across columns. Variation of RPT number down the rows.

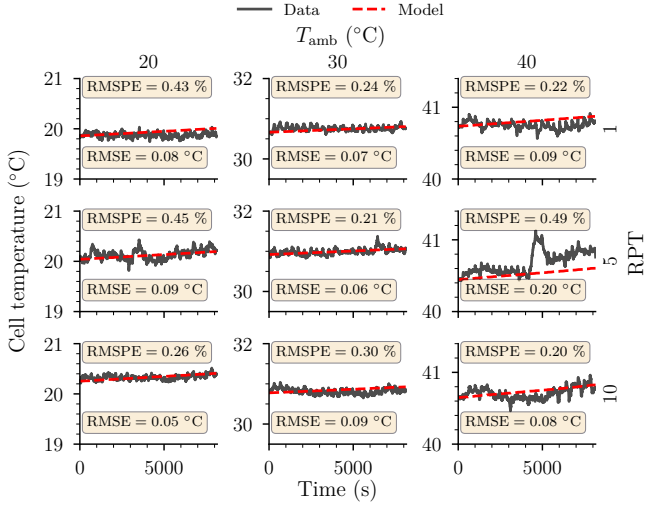


Fig. 17: We use the experimental temperature data to validate the thermal part of the single battery-cell model across a wide range of conditions. Every subplot shows the experimental (solid dark curve) and the model (dashed red curve) temperature as a function of time. Same condition variation as in Fig. 16

We observe that the identified model captures the voltage dynamics across a wide range of conditions with errors well underneath 1%. Similarly, we find that the identified model also captures the temperature dynamics across a wide range of conditions as seen in Fig. 17. The temperature errors are well beneath 1 °C.

APPENDIX V HIGH-FREQUENCY RESISTANCE AGING MODEL CALIBRATION

In order to calibrate the aging model, we use available experimental HPPC data (similar to the data shown in Fig. 6) obtained at different months of the experiment [1]. For each of these HPPC datasets, we calibrate the high-frequency resistance (HFR) of an cell ECM model (2) under the assumption that τ_1 and C_1 do not depend on aging. We know the discharge energy-throughput (4) corresponding to each HPPC taken and thus we can associate this discharge energy-throughput with the obtained HFR value. Having obtained these HFR values as a function of the discharge energy throughput, we compute the resistance increase

$$R_{\text{inc}}^{\%,\text{incr}}(\text{Wh}; \text{SoC}, T_{\text{amb}}) = \frac{R_0(\text{Wh}; \text{SoC}, T_{\text{amb}}) - R_0(0)}{R_0(0)} \quad (21)$$

The values obtained for (21) across the different months, or equivalently different discharge energy-throughput, is shown in Fig. 18.

Given these values, we scan across different values of the exponent in (7) and through nonlinear least-squares fitting, we obtain different values for the severity factor σ_{R_0} . We find that an exponent value of 1.05, fits the data best across all conditions. The severity factor values obtained then define a surface in the space of SoC and temperature

(red stars in Fig. 4). Equation (8) is then fit to these values using the CurveFitting toolbox in MATLAB. Having an expression for the severity factor and the exponent, we then evaluate (7). We find (Fig. 18) good agreement with the resistance increase values across most temperature conditions, and particularly at SoCs > 30%. In contrast, for SoC values < 30% the resistance increase trend is not as closely captured by the model likely originating from breakdown of the linear damage rule assumed in the models of the form (7). Nevertheless, even for these low SoCs, the general increase trend is captured adequately.

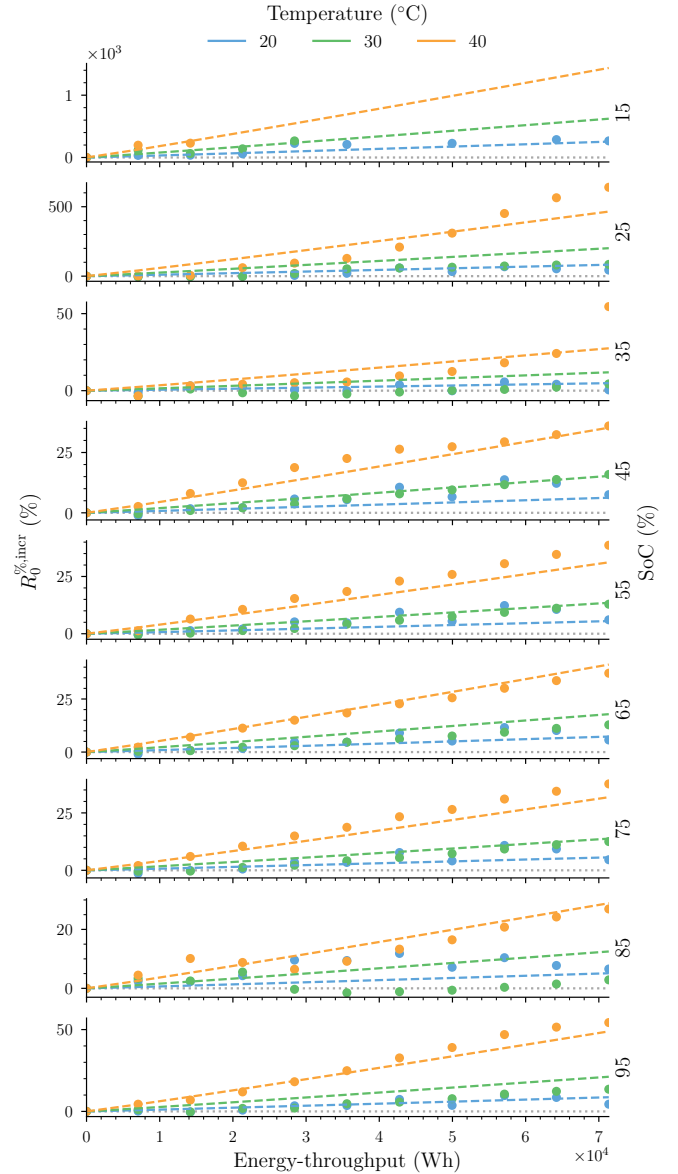


Fig. 18: High-frequency resistance increase aging data is described well by the proposed model. The points are obtained from calibrating an ECM model at various values of discharge energy-throughput of the cell and evaluating (21). The lines are obtained by evaluating (7) and (8) for the stated conditions.

REFERENCES

- [1] T. R. Tanim, M. G. Shirk, R. L. Bewley, E. J. Dufek, and B. Y. Liaw, "Fast charge implications: Pack and cell analysis and comparison," *Journal of Power Sources*, vol. 381, pp. 56–65, Mar. 2018.
- [2] R. Duarte, L. Moreira, L. A. M. Barros, V. Monteiro, J. L. Afonso, and J. G. Pinto, "Power Converters for a Small Islanded Microgrid Based on a Micro Wind Turbine and an battery energy storage system," in *ECOS 2018 Proceedings of the 31st International Conference on Eff. Cost, Optim. Simul. Environ. Impact Energy Syst.* (Guimarães, Portugal), 2018.
- [3] P. Wolfram and N. P. Lutsey, "Electric vehicles: Literature review of technology costs and carbon emissions," *International Council on Clean Transportation*, 2016.
- [4] W. Chen, J. Liang, Z. Yang, and G. Li, "A Review of Lithium-Ion Battery for Electric Vehicle Applications and Beyond," *Energy Procedia*, vol. 158, pp. 4363–4368, Feb. 2019.
- [5] R. Xiong, Q. Yu, W. Shen, C. Lin, and F. Sun, "A Sensor Fault Diagnosis Method for a Lithium-Ion Battery Pack in Electric Vehicles," *IEEE Trans. Power Electron.*, vol. 34, pp. 9709–9718, Oct. 2019.
- [6] S.-L. Jeng, C. M. Tan, and P.-C. Chen, "Statistical distribution of Lithium-ion batteries useful life and its application for battery pack reliability," *Journal of Energy Storage*, vol. 51, p. 104399, July 2022.
- [7] G. Plett, *Battery Management Systems, Volume I: Battery Modeling*. Artech House Power Engineering Series, Artech House, 2015.
- [8] A. Cordoba-Arenas, S. Onori, and G. Rizzoni, "A control-oriented lithium-ion battery pack model for plug-in hybrid electric vehicle cycle-life studies and system design with consideration of health management," *Journal of Power Sources*, vol. 279, pp. 791–808, Apr. 2015.
- [9] G. Suri and S. Onori, "A control-oriented cycle-life model for hybrid electric vehicle lithium-ion batteries," *Energy*, vol. 96, pp. 644–653, Feb. 2016.
- [10] F. Brosa Planella, W. Ai, A. M. Boyce, A. Ghosh, I. Korotkin, S. Sahu, V. Sulzer, R. Timms, T. G. Tranter, M. Zyskin, S. J. Cooper, J. S. Edge, J. M. Foster, M. Marinescu, B. Wu, and G. Richardson, "A continuum of physics-based lithium-ion battery models reviewed," *Prog. Energy*, vol. 4, p. 042003, Oct. 2022.
- [11] A. Allam and S. Onori, "Exploring the dependence of cell aging dynamics on thermal gradient in battery modules: A PDE-based time scale separation approach," in *2019 18th European Control Conference (ECC)*, (Naples, Italy), pp. 2380–2385, IEEE, June 2019.
- [12] Z. Wang, Z. Wang, J. Davidson, M. Foster, and D. Gladwin, "A Monte Carlo simulator to investigate cell-to-cell deviation in a grid-tied battery pack," *IET Power Electronics*, vol. 15, pp. 1264–1278, Oct. 2022.
- [13] J. Shin, W. Kim, K. Yoo, H. Kim, and M. Han, "Vehicular level battery modeling and its application to battery electric vehicle simulation," *Journal of Power Sources*, vol. 556, p. 232531, Feb. 2023.
- [14] G. Plett, *Battery Management Systems, Volume II: Equivalent-Circuit Methods*. Artech House power engineering and power electronics, Artech House, 2015.
- [15] X. Lin, H. E. Perez, S. Mohan, J. B. Siegel, A. G. Stefanopoulou, Y. Ding, and M. P. Castanier, "A lumped-parameter electro-thermal model for cylindrical batteries," *Journal of Power Sources*, vol. 257, pp. 1–11, July 2014.
- [16] S. Zhao and D. A. Howey, "Global Sensitivity Analysis of Battery Equivalent Circuit Model Parameters," in *2016 IEEE Vehicle Power and Propulsion Conference (VPPC)*, (Hangzhou, China), pp. 1–4, IEEE, Oct. 2016.
- [17] M. Shirk. private communication, 2023.